Shape-Controlled Fabrication of Micro/Nanoscale Triangle, Square, Wire-like, and Hexagon Pits on Silicon Substrates Induced by Anisotropic Diffusion and Silicide Sublimation

Huatao Wang,[†] Zhou Zhang,[†] Lai Mun Wong,[‡] Shijie Wang,[‡] Zhipeng Wei,[†] Gong Ping Li,[†] Guozhong Xing,[†] Donglai Guo,[†] Dandan Wang,[†] and Tom Wu[†,*]

[†]Division of Physics and Applied Physics, School of Physical and Mathematical Sciences, Nanyang Technological University, Singapore 637371, Singapore, and [‡]Institute of Materials Research and Engineering, 3 Research Link, Singapore 117602, Singapore

ABSTRACT We report the fabrication of micro/nanoscale pits with facile shape, orientation, and size controls on an Si surface *via* an Au-nanoparticles-assisted vapor transport method. The pit dimensions can be continuously tuned from 70 nm to several μm, and the shapes of triangles, squares, and wire/hexagons are prepared on Si (111), (100), and (110) substrates, respectively. This reliable shape control hinges on the anisotropic diffusivity of Co in Si and the sublimation of cobalt silicide nanoislands. The experimental conditions, in particular the substrate orientation and the growth temperature, dictate the pit morphology. On the basis of this understanding of the mechanism and the morphological evolution of the pits, we manage to estimate the diffusion coefficients of Co in bulk Si along the $\langle 100 \rangle$ and $\langle 111 \rangle$ directions, that is D_{100} and D_{111}. These diffusion coefficients show strong temperature dependence, for example, D_{100} is *ca*. 3 times larger than D_{111} at 860 °C, while they approach almost the same value at 1000 °C. This simple bottom-up route may help to develop new technologies for Si-based nanofabrication and to find potential applications in constructing nanodevices.

KEYWORDS: pits · morphology control · anisotropic diffusion · silicide

The silicon/metal interactions and the growth of various silicides are important for both fundamental sciences and modern silicon-based IC technologies.[1−5] In the conventional top-down lithography-based semiconductor processing, metal silicide thin films such as titanium silicide, nickel silicide, and cobalt silicide serve as indispensable components in microelectronic devices such as ohmic contacts, Schottky barrier contacts, gate electrodes, local interconnects, and so on.[1,6−8] As the device scaling proceeds with a relentless speed into the nanometer regime, deeper understandings of the silicon/metal interactions and the resulting silicides on the nanoscale are indispensable.[1,9] On another fast developing research front, bottom-up synthesized Si nanowires have been intensively exploited for their promising applications in electronics, optoelectronics, and biosensors.[10−12] From this perspective, well-defined nanoscale building blocks such as ohmic contacts and gates on individual Si nanowires must be developed and assembled into functional devices, which also requires systematic investigations on the interactions between Si and metals on the nanoscale.[13,14]

Propelled by the motivations delineated in the previous paragraph, there has been intensive interest in understanding the reactions between silicon and metals, especially the formation of silicides.[15−19] Among metal silicides, cobalt silicides possess very interesting and important properties, which has invited many research efforts, both fun-damental and application-oriented. Cobalt disilicide ($CoSi_2$) is widely used as a primary contact material in the metallization of Si-based integrated circuits, owing to its low resistivity (15−20 μohm·cm), low processing temperature, and good thermal stability.[1,20] There has been lots of research on the Si−Co systems, in particular on the issues of silicide formation, stability, and electrical transport.[21−36] For example, van Gurp and Langereis synthesized cobalt silicide layers by depositing Co onto Si wafers with subsequent thermal treatment and studied the Co diffusion in the silicide growth process.[37] Alberti *et al*. investigated the thermal stability of $CoSi_2$ and measured the relevant resistance.[38] However, so far there have been few studies focusing on the nanoscale Si−Co interaction.[8,39−41]
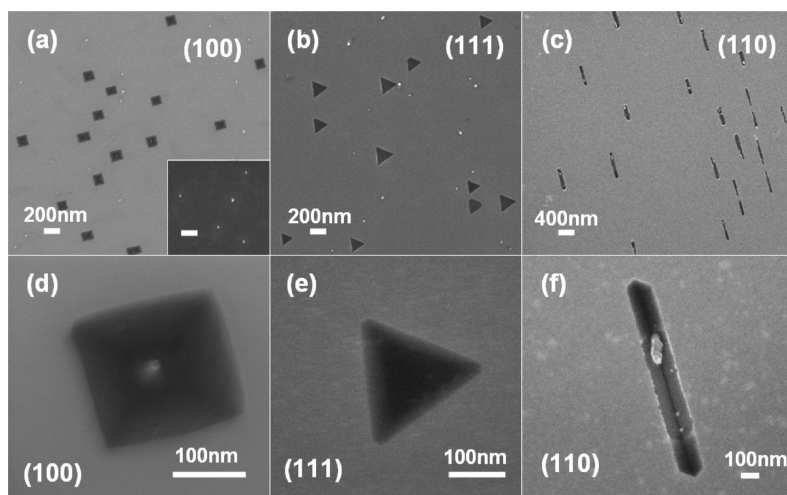
Figure 1. (a−c) SEM images of shape-controlled pits grown at 865 °C for 30 min using 30−40 nm Au NPs as catalyst. Square, triangle, and wire-shaped pits are fabricated on substrates of Si (100), Si (111), and Si (110), respectively. (d−f) Magnified SEM images of individual pits. The inset in panel A shows Au NPs on substrate before pits growth, and the scale bar corresponds to 200 nm.

Recently, Chen *et al*. investigated the growth kinetics of nanoscale Co silicide *via* point-contact reactions between Co nanodots and Si nanowires. They proposed that in such point-contact reactions the silicide formation is limited by the supply of Co atoms or the dissolution of Co into Si across the nanoscale contact.[42]

In this work, we report a quite unusual phenomenon related to the metal−silicon interaction. We used Au nanoparticles (NPs) as reacting centers to facilitate the nanoscale reaction between Si and Co. Interestingly, the anisotropic diffusion of Co in Si and the formation/subsequent sublimation of $CoSi_2$ nanoislands render morphology-controlled nanopits on Si substrates. Triangle, square, and wire/hexagon shaped nanopits were obtained on Si (111), (100), and (110) substrates, respectively. Furthermore, by systematically investigating the effects of substrate orientation and synthesis temperature on the morphology of the nanopits, the diffusion coefficients of Co in bulk Si along the $\langle 100 \rangle$ and $\langle 111 \rangle$ directions were simultaneously determined and compared. This synthesis of inverted nanostructures in Si with facile morphology control complements the existing literature on free-standing silicide nanowires grown on top of Si substrates. Our study adds to the rich phenomena in the Si-metal systems and may help to facilitate the construction of functional Si-based nanodevices.

RESULTS AND DISCUSSION

Morphology-Controlled Pits on Silicon Surface. Figure 1a−c shows representative SEM images of samples grown at 865 °C for 30 min. We should note here that in general the synthesis temperature was intentionally set much higher than what is usually used for silicides growth.[34,35,37] It was found that the substrate orientation and symmetry reproducibly dictate the shape of the inverted nanostructures. Nanopits in shapes of tri-

angles, squares, and wire were observed on Si (111), (100), and (110) substrates, respectively, and all the nanopits have the same orientation in a given sample. The equilateral square and triangle pits exhibit lateral dimensions from 80 to 230 nm and from 75 to 210 nm, respectively. The wire-shaped pits have widths between 95 and 220 nm, and lengths between 400 and 1300 nm. In general, by carefully adjusting the reaction temperature and duration, we can reproducibly control the dimension of the pits from under 70 nm to several μm. Typical high-magnification SEM images of these pits (Figure 1d−f) reveal that their corners are quite sharp, while small islands were often observed at the centers. Further observations on the cross sections of pits grown at 940 °C for 10 min indicate that the exposed inner walls are not smooth, but covered with many nanoislands (Figure 2a−c).

By examining their angles relative to the substrate coordinates (Supporting Information, Table S1), the exposed surfaces for pits can be identified (Supporting Information, Figures S2, S3).[43,44] In particular, as shown in Figure 2d, the four sidewalls of square pits formed on Si (100) substrate are (111), (1$\bar{1}$1), (1$\bar{1}$$\bar{1}$), and (11$\bar{1}$), respectively, with the edges along Si $\langle 011 \rangle$, $\langle 01\bar{1} \rangle$, $\langle 0\bar{1}\bar{1} \rangle$, and $\langle 0\bar{1}1 \rangle$. In the cross-sectional TEM image of the square pits (Supporting Information, Figure S2), the sidewall planes form an angle of 54.7° with the bottom, which matches well with the angle between Si (111)/(1$\bar{1}$1) and Si (100) planes. For triangle pits, the three exposed planes are ($\bar{1}$11), (1$\bar{1}$1), and (11$\bar{1}$) with the edges along Si $\langle \bar{1}10 \rangle$, $\langle 0\bar{1}1 \rangle$, and $\langle \bar{1}01 \rangle$ (Figure 2e). For wire-shaped pits, the exposed planes at two ends are (100) and (010), and the two sidewalls are (111) and (11$\bar{1}$), with the edges along Si $\langle \bar{1}10 \rangle$ and $\langle 1\bar{1}0 \rangle$ (Figure 2f, also see Supporting Information, Figure S3 for more details). The inset images in Figure 2d−f show the cross-sectional schematics of the square, triangle, and wire-shaped
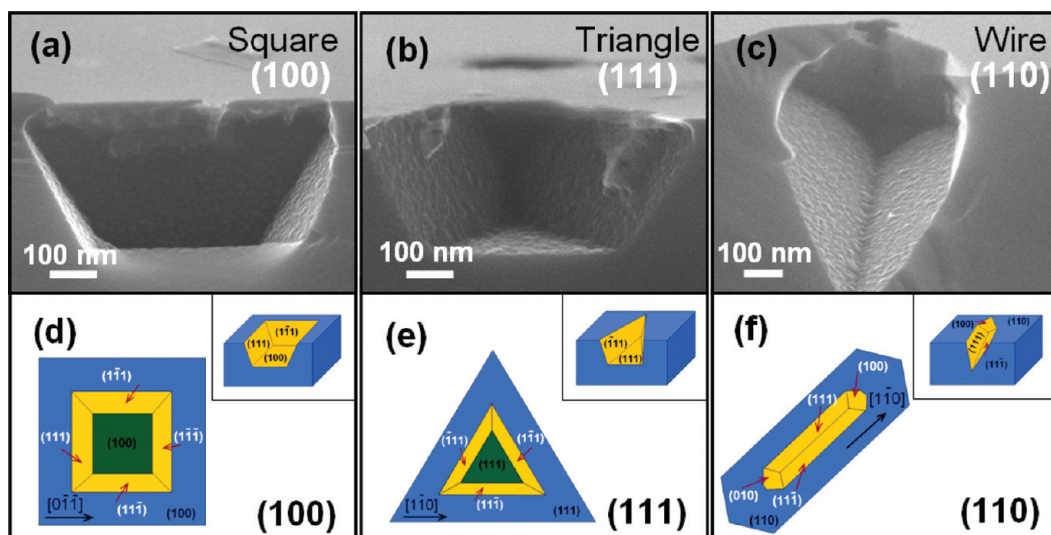
Figure 2. (a−c) Cross-sectional SEM images of square, triangle, and wire-shaped pits grown on Si substrates at 910 °C for 10 min. (d−f) Schematic diagrams showing orientations of the exposed walls of square, triangle, and wire-shaped pits. The insets are the corresponding 3D cross-sectional schematics.

pits. Notably, Si {111} is the most frequent exposed plane in nanopits: for square and triangle nanopits, all the exposed side planes belong to {111}; for wire-shaped nanopits, the broad sidewalls also belong to {111}. This observation is not surprising from the viewpoint of thermodynamics: {111} planes have the minimum surface energy among all the crystalline planes in Si.[44−46] Therefore, these planes are more stable than the others and often exposed after wafer processing such as dry or chemical etching.

Morphology Formation and Evolution Mechanism. Formation and evolution of the nanopits were systematically investigated by comparing the products obtained at various synthesis stages. At the beginning, Au NPs melt on Si (Figure 3a,e,i), and then nanopits with rounded corners gradually appear (Figure 3b,f,j). With increasing reaction time, the nanopits expand continuously, and their depth also increases. In addition to the dimension change, the morphology of the nanopits simultaneously evolves; that is, they gradually become more well-defined with sharper corners in the later growth stages (Figure 3c,g,k). Interestingly, the wire-shaped nanopits appear almost isotropic at the initial stage (Figure 3j), similar to the triangle and square pits, but
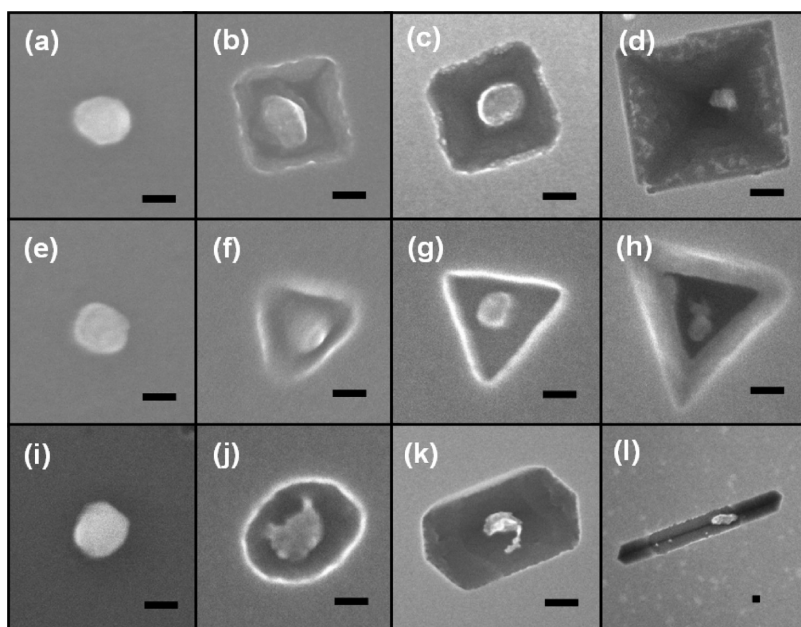

Figure 3. Morphology evolution of nanopits at various synthesis stages. SEM images illustrating the nanopits formation process on Si (100) (a−d), Si (111) (e−h) and Si (110) (i−l) obtained at a synthesis temperature of 865 °C. In panels a−d, the time durations held at the synthesis temperature are 2, 5, 10, and 20 min, respectively. In panels e−h, they are 3, 7, 12, and 20 min, respectively. In panels i−l, they are 1, 5, 12, and 30 min, respectively. In all images, the scale bars correspond to 30 nm.
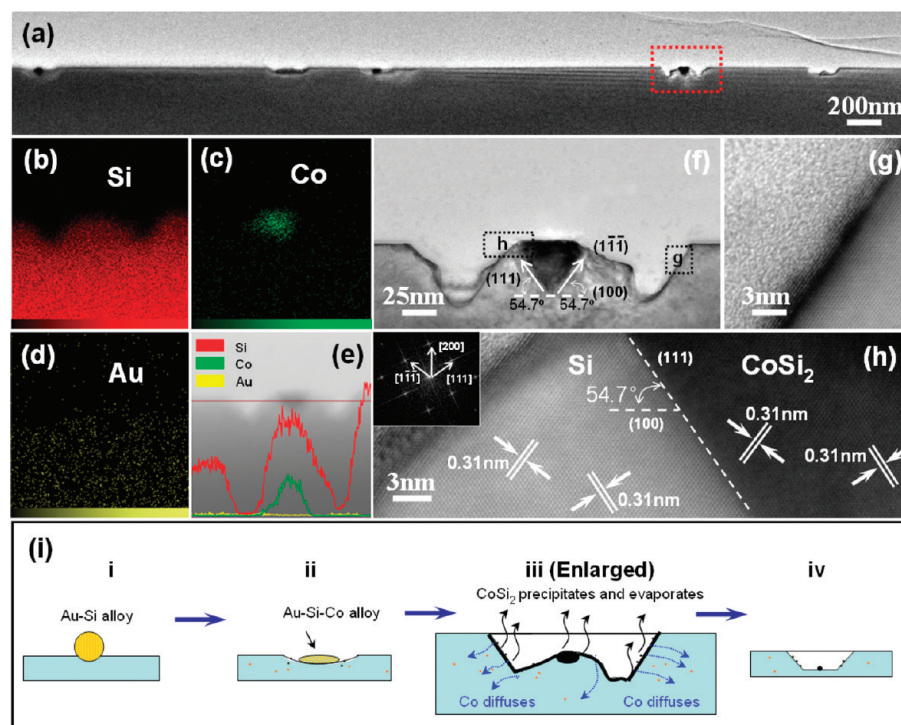
Figure 4. Cross-sectional TEM and EDS data for square nanopits on Si (100). The synthesis took place at 910 °C and was terminated at an intermediate stage after 8 min, before the complete nanopits formation. (a) Cross-sectional TEM image. Panels b, c, and d show EDS mappings of elements Si, Co, and Au, respectively. (e) The corresponding EDS line mappings. (f) Enlarged TEM image from the selected area in panel a. (g) HRTEM image of the highlighted area in panel f. HRTEM image and fast Fourier transform pattern in panel h show the interface of Si/CoSi$_2$. (i) Schematic illustrating the nanopits formation mechanism including (i) forming of Au−Si alloy; (ii) absorbing Co vapor to form Au−Si−Co alloy; (iii) diffusion of Co in Si, leading to the precipitation of CoSi$_2$, and the subsequent sublimation of CoSi$_2$ at high temperatures; (iv) finally formed nanopits.

they extend rapidly in the length directions during the later stages (Figure 3k), eventually gaining the wire-like morphology with high anisotropy (Figure 3l). It should be noted that there are usually islands at the nanopits centers, which are presumably the same positions as the initial Au NPs. These islands shrink with increasing synthesis time, and they eventually become almost invisible after growing for 20−30 min (Figure 3d,h,i).

To reveal the formation mechanism, detailed cross-sectional TEM and EDS analyses were carried out. A sample on Si (100) with pits formed at an intermediate stage (910 °C for 8 min) was thinned with conventional TEM sample preparation techniques. Figure 4a is a low magnification TEM image, showing several incomplete pits formed on the Si substrate surface. As shown in the highlighted area, there is obvious contrast between the center area (the triangle island) and the background. Figure 4f is an enlarged TEM image of this area. The triangle island at the center appears much darker than the surrounding area, indicating different compositions. Indeed, the EDS element mappings confirm that the darker triangle island is rich in Co and Si, presumably CoSi$_2$, while the surrounding area is almost pure Si (Figure 4b−e).

A high-resolution transmission electron microscope (HRTEM) image along the CoSi$_2$/Si interface (Figure 4h) indicates two interplane distances of 0.31/0.31 nm,

which agrees well with lattice constants of the face-centered cubic CoSi$_2$ (JCPDS: 38-1449). The fast Fourier transform (FFT) pattern in the inset of Figure 4h also suggests that the black triangle island in the center is indeed composed of CoSi$_2$. The CoSi$_2$ island appears to grow epitaxially into the Si (100) substrate. Further characterizations indicate that the CoSi$_2$ island has a particular orientation with respect to the substrate, sharing a (111) interface with the Si surface.[34] It is not surprising that CoSi$_2$ with a CaF$_2$ structure shares an epitaxial relationship with Si since the lattice mismatch between them is only 1.2% at room temperature.[47] Similar to previous reports,[47,48] no obvious defects were found at the CoSi$_2$/Si interface. Supporting Information, Figure S8 provides more TEM images taken at the interface regions which confirm that both types of interfaces are along {111} with the same orientation and small lattice mismatch. It is well-known that epitaxial growth of CoSi$_2$ on Si (111) and (100) can be achieved by simply heating Co thin films deposited on Si at low temperatures, and CoSi$_2$ islands with {111} planes are preferably formed, where Co diffusion in Si plays a crucial role.[48,49] Importantly, pinholes were often found on the surfaces of CoSi$_2$ islands, which has not been thoroughly investigated.[47,48,50] We believe that these pinholes are highly related to the nanopits formation in our experiments, as we will discuss later. Figure 4g is another

HRTEM image, highlighting the coarse-grained thin film covering the sidewalls with a thickness of 2 ± 0.5 nm. Although EDS cannot determine the thin film composition due to the resolution limit, it is presumably Co rich since it appears darker than the adjacent Si area.

On the basis of the above microscopic results, we propose the following mechanism for the nanopits formation, which is illustrated in Figure 4i. According to the Au−Si binary phase diagram, at temperatures as low as 300−400 °C, Au NPs already start forming Au−Si alloys with the Si substrate, (Figure 4i, part i).[51] With the synthesis temperature rising beyond ~800 °C, cobalt oxide in the source powder is reduced by graphite to generate Co vapor, which is then absorbed by the Au−Si alloy to form Au−Si−Co alloy nanoparticles (Figure 4i, part ii). As the substrate temperature rises beyond 850 °C, $CoSi_2$ gradually precipitates from the Au−Si−Co alloy due to its higher stability. The main driving force for the Co diffusion and the $CoSi_2$ formation is the concentration gradient of Co in Si, which is quite high since the Co-containing layer is only ~2 nm as indicated in the TEM image in Figure 4g. In other words, the $CoSi_2$ precipitation and formation hinge on the continuous supply of the Co vapor as well as the diffusion of Co through the exposed Si planes. At temperatures above 860 °C and ambient pressure of 1−20 mbar, the sublimation of the $CoSi_2$ phase effectively erodes the periphery area of the central island and the exposed nanopits walls (Figure 4i, part iii). Our results suggest that the melting point of the nanoscale $CoSi_2$ is much lower than the bulk value of 1326 °C owing to the remarkable size effect in nanostructures.[52] In addition, $CoSi_2$ is prone to decompose at temperatures higher than its thermal stability temperature of 900 °C.[53] In the synthesis, Si is continuously consumed by reacting with Co to form $CoSi_2$ and the sublimation of $CoSi_2$ eventually leads to the formation of well-defined nanopits (Figure 4i, part iv). The observations of tiny $CoSi_2$ islands in the nanopits (Figure 4f) and the coarse grained thin films covering the exposed planes (Figure 2a−c) strongly support this proposed formation mechanism.

It is true that the diffusion of Co in Si also contributes to the pits formation. However, we did not find much Co or cobalt silicide inside the pits walls except a ~2 nm Co-rich layer. Therefore, the formation and sublimation of $CoSi_2$ appear to be the dominant factor for the pits formation, and we can exclude the diffusion of Co into Si as the main driving force. Nevertheless, Co diffusion driven by the concentration gradient is the prerequisite for the silicide formation, therefore playing an important role.

Regarding the growth anisotropy, there have been reports on silicides nanowires formed when heating metals deposited on Si substrates, and the different growth rates of length and width were often attributed to the anisotropic lattice mismatch between silicides and Si.[15,54,55] However, the $CoSi_2$/Si mismatch in our case is quite small (only 1.2%, and $CoSi_2$ and Si have the same cubic crystal structure, JCPDS: 38-1449 and 27-1402, respectively).[47] Furthermore, the two types of interfaces (Figure 4 and Supporting Information, Figure S8) exhibit the same lattice mismatch and the epitaxial relationship is $CoSi_2$ (111)/Si (111) and $CoSi_2$ ($1\bar{1}\bar{1}$)/Si ($1\bar{1}\bar{1}$), suggesting that the interfaces in our system are symmetrical instead of the previously reported asymmetric interfaces.[15] This symmetry of interfaces directly affects the anisotropy growth due to the strain effect.[15,56] Thus we believe that there must be other factors dictating the morphology of micro/nanostructures formed on an Si substrate besides the anisotropic lattice mismatch between silicide and Si. In a recent study, He *et al.* presented a physical mechanism for the formation of self-assembled dysprosium silicide nanowires, which involves a low-energy coherent interface instead of an anisotropic lattice mismatch.[57] In systems with a small isotropic lattice mismatch such as $DySi_2$/Si and $CoSi_2$/Si, coherent interfaces may form on both sides of silicide islands, which adds coherent strain to the islands and possibly leads to the anisotropic growth.[57] These results suggest that large lattice mismatch is not always required for the formation of anisotropic silicide nanostructures.

As to the shape dependence on the substrate orientation, existing literatures have documented silicide islands or clusters with various shapes formed when depositing metals on Si substrates followed by annealing. Examples are triangular silicide nanoislands formed on Si (111),[15] manganese silicide nanowires and islands on Si (111),[58] square-shaped $NiSi_2$ islands on Si (100),[59,60] and $CoSi_2$ quantum dots formed on Si (111).[61] Zhang *et al.* concluded that triangle, square, and wire-like Cu_3Si nanostructures can grow depending on the orientation of silicon substrates.[5] Moreover, Qiao *et al.* found that the shape of etched nanostructures can be controlled by the Si substrates orientation,[43] which is in line with studies on anisotropic etching of silicon.[62−64] Therefore, it is quite universal that the orientation of Si substrates has great influence on the morphology of micro/nanostructures formed on the Si surface.

We should note here that pits (pinholes) formation is a phenomenon often found in metal silicides such as Ni−Si, Y−Si, Co−Si, and Dy−Si, which is usually attributed to the localized depletion of Si atoms.[47,65−67] In contrast, the sublimation of $CoSi_2$ plays the critical role in the formation mechanism proposed here. More importantly, our results provide a facile Au-nanoparticles-assisted vapor-based route to produce nanopits on silicon surfaces. It is well-known that the fabrication of sub-100 nm features on silicon surfaces is a critical challenge for a wide range of future silicon-based technologies.[43] Although the top-down photolithography techniques have seen decades of remarkable improvements, alternative strategies to produce nanoscale silicon architectures are currently under intense
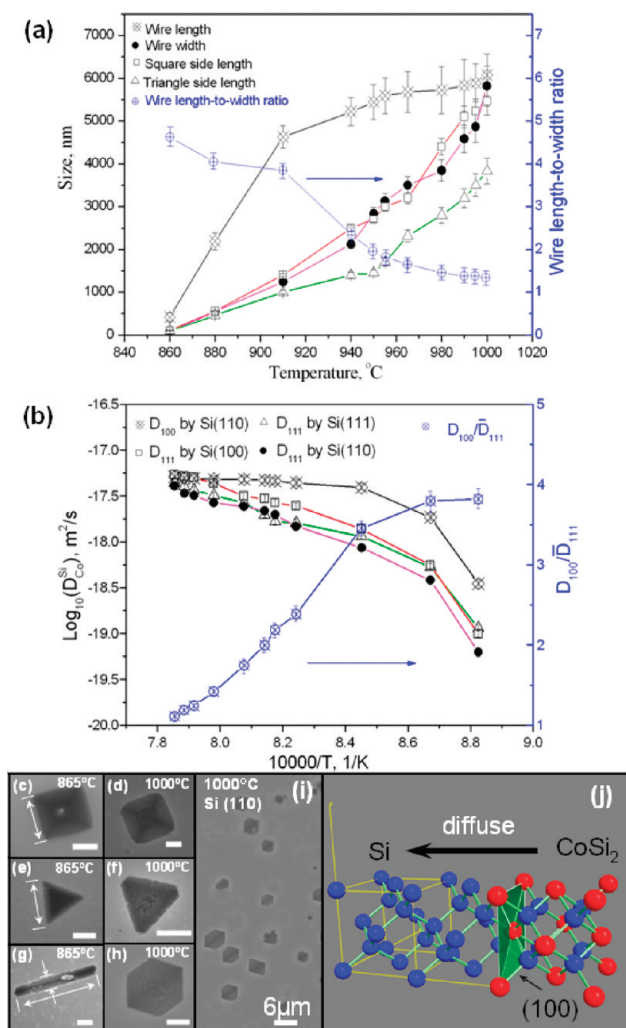
Figure 5. (a) Variations of pits sizes after growth at 860−1000 °C for 30 min. Also shown is the data of length-to-width ratio of wire-like pits. (b) Measured diffusion coefficients of Co in bulk Si along ⟨100⟩ and ⟨111⟩ at 860−1000 °C and ratio of D_{100} to D_{111}, revealing anisotropic Co diffusion in Si and its dependence on temperature. (c−i) Typical SEM images of pits formed on Si (100), (111), and (110) at 865 and 1000 °C. (j) Schematic diagram of Co diffusion in Si along ⟨100⟩ with the formation of $CoSi_2$. The scale bars in panels c, e, that in panel g, and those in panels d,f, h correspond to 100, 150, and 2 μm, respectively.

pursuits.[43,68] In the method delineated here, the shape of pits can be readily controlled by the Si substrate orientation. Furthermore, as we will discuss below, the pits dimension can be well adjusted by the synthesis temperature and time. Potentially, this bottom-up facile approach may also give control on the positions of individual nanopits by manipulating the Au nanoparticles. Other advantages of this method include simple processing and less contamination compared to the conventional plasma-assisted dry etch technique.[69]

We also should take note of the critical role of the Au NPs in the pits formation. In our experiments, Au NPs were used as the catalyst to initiate the reaction between Co and Si at the nanoscale, therefore serving as reacting centers. They were found to be crucial for the formation of pits; controlled experiments without Au

NPs did not give any regular pits (Supporting Information, Figure S5). However, EDS data in Figure 4c,e show no Au-rich area, which may be attributed to the fast migration and evaporation of Au at high temperatures.[70,71]

Determination of the Diffusion Coefficients of Co in Si. In the proposed mechanism, the diffusion of Co in bulk Si is an essential ingredient.[72] By examining the growth rates of triangle, square, and wire-shaped pits, the anisotropic diffusivities of Co in bulk Si can be quantitatively investigated. To carry out the calculations, four characteristic dimensions are defined in Figure 5c,e,g, namely, the length and the width of the wire-shaped pits, and the side lengths of the square and the triangle pits. At a synthesis temperature of 880 °C these dimensions increase almost linearly with the synthesis time which was varied from 5 to 30 min (Supporting Information, Figure S7). Interestingly, the side length of the square and the triangle pits and the width of the wire-shaped pits grow with similar rates; however, the length of the wire-shaped pits increases 4−5 times faster. This contrast can be attributed to the fact that the growth fronts of the square and the triangle pits and the side walls of the wire-shaped pits propagate along Si ⟨111⟩, while the ends of the wire-shaped pits form along Si ⟨100⟩ (Figure 2 and Supporting Information, Figure S2). Therefore, the growth rates of pits along the four defined dimensions ($v_{length-wire}$, $v_{width-wire}$, v_{square}, and $v_{triangle}$) can be determined. Combined with the angular relationship between the Si lattice and the diffusion planes ($\theta_{(100)/(110)}$, $\theta_{(111)/(110)}$, $\theta_{(111)/(100)}$, and $\theta_{(11\bar{1})/(111)}$), Co diffusion rates ($v_{\langle100\rangle}$, $v_{\langle111\rangle}$) along Si ⟨100⟩ and ⟨111⟩ on (110), (100), and (111) substrates were calculated. The corresponding diffusion coefficients (D_{100}, D_{111}) were estimated based on the Fick's first law:

$$J = -D\frac{\partial C}{\partial x} \tag{1}$$

where the diffusion flux J is the number of atoms crossing a unit area per second and $\partial C/\partial x$ is the gradient of the concentration C (number of atoms per unit volume).[73,74] Co diffusion can be considered as steady state owing to the stable, continuous, and rich supply of Co vapor; that is, $\partial C/\partial x$ remains a constant. Therefore, the number of Co atoms (n) crossing unit area (S) during time t can be described as[36,75−77]

$$n = JSt = -D\frac{\partial C}{\partial x}St \tag{2}$$

from which the diffusion coefficients can be estimated (see the Supporting Information for calculation details).

Figure 5a shows the change of the size of the pits as well as the length-to-width ratio of the wire-shaped pits after being grown for 30 min at several temperatures between 860 and 1000 °C. Figure 5b shows the temperature dependence of D_{100} and D_{111} as well as the ratio of D_{100} to $\bar{D}_{(111)}$. It is important to note that there

is only one way to calculate D_{100} based on the temperature-dependent length variation of the wire-shaped pits, while there are three ways to calculate D_{111} by examining the temperature dependence of the width variation of the wire-shaped pits and the side length variations of the square and the triangle pits. The three groups of D_{111} have a similar order of magnitude due to the identical diffusion process along Si $\langle 111 \rangle$, and their average values give $\bar{D}_{(111)}$.

Notably, D_{100} is much larger than D_{111} at 860−940 °C, and their difference shrinks as the temperature increases and almost disappears at 1000 °C. $D_{100}/\bar{D}_{111}$ is as high as 3−4 at 860−910 °C, and then decreases to 1.1−1.4 at 980−1000 °C. These data clearly disclose the strong temperature dependence of the Co diffusion in Si, which is linked with the anisotropy of the Si crystal structure. The anisotropy of diffusion becomes weaker at high temperatures owing to the accelerated isotropic lattice vibration. The anisotropic diffusion of Co in the bulk Si directly determines the shape of the pits. In particular, because the three exposed planes of $(\bar{1}11)/(1\bar{1}1)/(11\bar{1})$ in the triangle pits belong to the same {111} group, Co diffuses through these planes with the same rate, leading to the formation of the triangle-shaped pits on Si (111). Similarly, the equivalence of the $(111)/(1\bar{1}1)/(1\bar{1}\bar{1})/(11\bar{1})$ planes results in the formation of square pits on Si (100). The situation is more complex on Si (110): two kinds of planes, that is, {100} and {111}, are exposed in the wire-shaped pits. At relatively lower temperature, for example, 860 °C, the larger diffusion coefficient of Co along Si $\langle 100 \rangle$ causes faster formation and sublimation of $CoSi_2$ than that along $\langle 111 \rangle$. Thus pits on Si (110) extend longer along $\langle 100 \rangle$ than $\langle 111 \rangle$, leading to the wire-like shape (Figure 5g). At higher temperatures, for example, 1000 °C, D_{100} and D_{111} are almost equal, leading to the formation of hexagonal pits (Figure 5h,i).

Although many efforts have been devoted to investigate the metal diffusivities in Si, to our best knowledge, it is the first time that the temperature-dependent diffusion coefficients of Co along Si $\langle 111 \rangle$ and $\langle 100 \rangle$ are simultaneously estimated.[23,25,36,77−81] Appelbaum et al. studied subsurface Co diffusion in Si (100) using radioactive tracer and SIMS analytical techniques and concluded that the relevant diffusion coefficients were in the range of 10^{-20} to 10^{-19} m^2/s at 860−1000 °C.[23] Our results are higher than theirs (D_{100} equals to 3.50×10^{-19} and 5.10×10^{-18} m^2/s at 860 and 1000 °C, respectively), but fall in a similar order of magnitude (See Table S2 in the Supporting Information). This discrepancy may be due to the different experimental methods, and further comparative studies are needed.

CONCLUSIONS

Micro/nanoscale pits on Si substrates with long-range ordering and reliable shape control have been fabricated via a facile vapor transport method assisted by Au NPs. Pits in shapes of triangles, squares, and wire/hexagon were obtained on Si (111), (100), and (110) substrates, respectively, which were mainly determined by the substrate orientation and temperature. In our proposed growth mechanism, anisotropic Co diffusion in Si and sublimation of cobalt silicide nanoislands play deterministic roles in the formation of the pits. The temperature dependent diffusion coefficients of Co in Si along $\langle 111 \rangle$ and $\langle 100 \rangle$ was estimated and compared. At a relatively lower temperature of 860 °C, D_{100} is ∼3 times larger than D_{111}, while they have almost the same value at higher temperatures. This facile approach to fabricate nanopits on Si substrate with controlled shape and size may find potential applications in constructing nanodevices due to its good nanoscale morphology controls and simple processing. We also expect this simple method to be generalized to carry out the nanoscale machining/engineering of other semiconductor surfaces.

METHODS

Synthesis of Pits in Shape of Triangles, Squares, Wires, and Hexagons. Our experiments were carried out in a home-built vapor transport growth system comprising a quartz tube heated by a horizontal tube furnace (Lindberg/Blue Mini-Mite) (Supporting Information, Figure S1). Si wafers with (111), (100), and (110) orientations were cut into small pieces with a typical size of 6 × 6 mm and cleaned by ultrasonication in ethanol. To obtain uniform distribution of Au NPs, the substrates were pretreated with oxygen plasma to render superhydrophilic surfaces. During the substrate preparation, no HF etching was used. Au NPs with the size of 30−40 nm were dispersed on the substrate surfaces and dried in air.[5] A mixed powder of cobalt oxide (Aldrich 99.99%) and graphite (Riedel-de Haën) with a total weight of 0.03 g and a weight ratio of 1:1 was used as the Co source. In the furnace tube, the silicon substrates were placed 3−10 cm downstream from the source powder. Ar was introduced as the carrying gas with a constant flow rate of 100 sccm and the pressure inside the quartz tube was maintained at 1−20 mbar. To achieve reproducible synthesis, the source and the substrate temperatures in the range of 800−1000 °C were carefully calibrated. The synthesis temperature was intentionally set much higher than what is usually used for silicides growth.[34,35,37] The furnace tube was heated for a predetermined period of time and then quickly cooled down to room temperature.

Characterizations. A JEOL JSM-6700F field emission scanning electron microscope (SEM) and a JEOL 2100 high resolution transmission electron microscope (HRTEM) were used to study the sample morphology and structure. The composition was determined by energy dispersive X-ray spectrometers (EDS) attached to the TEM. Atomic force microscopy (AFM) study was carried out on a D3100 V system from Veeco.

Supporting Information Available: Calculation of diffusion coefficients of Co in bulk Si along the $\langle 111 \rangle$ and $\langle 100 \rangle$ directions, the comparisons between our results and other results on Co dif-

fusion coefficients, experimental setup, the identification of the pits' exposed planes and others. This material is available free of charge *via* the Internet at http://pubs.acs.org.

REFERENCES AND NOTES

1. Chen, L. J. Metal Silicides: An Integral Part of Microelectronics. *J. Oper. Manage.* **2005**, *57*, 24–30.
2. Dong, L. F.; Bush, J.; Chirayos, V.; Solanki, R.; Jiao, J. Dielectrophoretically Controlled Fabrication of Single-Crystal Nickel Silicide Nanowire Interconnects. *Nano Lett.* **2005**, *5*, 2112–2115.
3. Schmitt, A. L.; Bierman, M. J.; Schmeisser, D.; Himpsel, F. J.; Jin, S. Synthesis and Properties of Single-Crystal FeSi Nanowires. *Nano Lett.* **2006**, *6*, 1617–1621.
4. Hsu, H. C.; Wu, W. W.; Hsu, H. F.; Chen, L. J. Growth of High-Density Titanium Silicide Nanowires in a Single Direction on a Silicon Surface. *Nano Lett.* **2007**, *7*, 885–889.
5. Zhang, Z.; Wong, L. M.; Ong, H. G.; Wang, X. J.; Wang, J. L.; Wang, S. J.; Chen, H. Y.; Wu, T. Self-Assembled Shape- and Orientation-Controlled Synthesis of Nanoscale Cu_3Si Triangles, Squares, and Wires. *Nano Lett.* **2008**, *8*, 3205–3210.
6. Song, Y. P.; Schmitt, A. L.; Jin, S. Ultralong Single-Crystal Metallic Ni_2Si Nanowires with Low Resistivity. *Nano Lett.* **2007**, *7*, 965–969.
7. Stiufiuc, R.; Soubiron, T.; Grandidier, B.; Deresmes, D. Electronic and Structural Properties of Titanium Silicide Nanostructures Formed on Si (111) 7×7 Reconstructed Surface. *J. Optoelectron. Adv. Mater.* **2007**, *9*, 591–594.
8. Tedesco, J. L.; Rowe, J. E.; Nemanich, R. J. Conducting Atomic Force Microscopy Studies of Nanoscale Cobalt Silicide Schottky Barriers on Si(111) and Si(100). *J. Appl. Phys.* **2009**, *105*, 7.
9. Li, B.; Luo, Z. Q.; Shi, L.; Zhou, J. P.; Rabenberg, L.; Ho, P. S.; Allen, R. A.; Cresswell, M. W. Controlled Formation and Resistivity Scaling of Nickel Silicide Nanolines. *Nanotechnology* **2009**, *20*, 085304.
10. Cui, Y.; Lieber, C. M. Functional Nanoscale Electronic Devices Assembled Using Silicon Nanowire Building Blocks. *Science* **2001**, *291*, 851–853.
11. Cui, Y.; Wei, Q. Q.; Park, H. K.; Lieber, C. M. Nanowire Nanosensors for Highly Sensitive and Selective Detection of Biological and Chemical Species. *Science* **2001**, *293*, 1289–1292.
12. Cui, Y.; Zhong, Z. H.; Wang, D. L.; Wang, W. U.; Lieber, C. M. High-Performance Silicon Nanowire Field Effect Transistors. *Nano Lett.* **2003**, *3*, 149–152.
13. Stern, E.; Cheng, G.; Klemic, J. F.; Broomfield, E.; Turner-Evans, D.; Li, C.; Zhou, C.; Reed, M. A. Methods for Fabricating Ohmic Contacts to Nanowires and Nanotubes. *J. Vac. Sci. Technol., B* **2006**, *24*, 231–236.
14. Weber, W. M.; Geelhaar, L.; Graham, A. P.; Unger, E.; Duesberg, G. S.; Liebau, M.; Pamler, W.; Cheze, C.; Riechert, H.; Lugli, P.; *et al.* Silicon-Nanowire Transistors with Intruded Nickel-Silicide Contacts. *Nano Lett.* **2006**, *6*, 2660–2666.
15. He, Z. A.; Smith, D. J.; Bennett, P. A. Endotaxial Silicide Nanowires. *Phys. Rev. Lett.* **2004**, *93*, 4.
16. George, T.; Fathauer, R. W. Endotaxial Growth of $CoSi_2$ within (111) Oriented Si in a Molecular-Beam Epitaxy System. *Appl. Phys. Lett.* **1991**, *59*, 3249–3251.
17. Wu, L. H.; Tsai, C. J. Surface Cleanness Dependence of the Interfacial Orientation of Endotaxial $NiSi_2$ on Si(001). *Electrochem. Solid State Lett.* **2009**, *12*, H73–H76.
18. Liang, S.; Islam, R.; Smith, D. J.; Bennett, P. A. Phase Transformation in $FeSi_2$ Nanowires. *J. Cryst. Growth* **2006**, *295*, 166–171.
19. Fathauer, R. W.; George, T. Growth-Parameters Affecting the Formation of Buried $CoSi_2$ by Endotaxy of Co on Si(111). *J. Vac. Sci. Technol., A* **1992**, *10*, 2404–2406.
20. Kluth, P.; Zhao, Q. T.; Winnerl, S.; Lenk, S.; Mantl, S. Fabrication of Epitaxial $CoSi_2$ Nanowires. *Appl. Phys. Lett.* **2001**, *79*, 824–826.
21. Seo, K.; Varadwaj, K. S. K.; Mohanty, P.; Lee, S.; Jo, Y.; Jung, M. H.; Kim, J.; Kim, B. Magnetic Properties of Single-Crystalline CoSi Nanowires. *Nano Lett.* **2007**, *7*, 1240–1245.
22. Weber, E. R. Transition-Metals in Silicon. *Appl. Phys. A: Mater. Sci. Process.* **1983**, *30*, 1–22.
23. Appelbaum, A.; Malm, D. L.; Murarka, S. P. Subsurface Cobalt Diffusion in Silicon Single-Crystal from Infinitesimally Small Cobalt Diffusion Source. *J. Vac. Sci. Technol., B* **1987**, *5*, 858–864.
24. Chevallier, J.; Larsen, A. N. Epitaxial Nickel and Cobalt Silicide Formation by Rapid Thermal Annealing. *Appl. Phys. A: Mater. Sci. Process.* **1986**, *39*, 141–145.
25. Botha, A. P.; Kritzinger, S.; Pretorius, R. Self-Diffusion of Silicon in Thin-Films of Cobalt, Nickel, Palladium, and Platinum Silicides. *Thin Solid Films* **1986**, *141*, 41–51.
26. Murarka, S. P. Codeposited Silicides in Very-Large-Scale Integration. *Thin Solid Films* **1986**, *140*, 35–50.
27. Murarka, S. P.; Vaidya, S. Cosputtered Cobalt Silicides on Silicon, Polycrystalline Silicon, and Silicon Dioxide. *J. Appl. Phys.* **1984**, *56*, 3404–3412.
28. Chen, B. S.; Chen, M. C. Thermal-Stability of Cobalt Silicide Thin-Films on Si(100). *J. Appl. Phys.* **1993**, *74*, 1035–1039.
29. Comrie, C. M.; Newman, R. T. Dominant Diffusing Species during Cobalt Silicide Formation. *J. Appl. Phys.* **1996**, *79*, 153–156.
30. Lexa, D.; Kematick, R. J.; Myers, C. E. Thermodynamics of Phase Formation of the Cobalt Silicides. *Chem. Mater.* **1996**, *8*, 2636–2642.
31. Nygren, S.; Caffin, D.; Ostling, M.; Dheurle, F. M. In *Morphological Instabilities of Nickel and Cobalt Silicides on Silicon*, 4th European Workshop on Refractory Metals and Silicides (Rms 1991), Saltsjobaden, Sweden, Mar 24−27, 1991; Elsevier Science Bv: Saltsjobaden, Sweden, 1991; pp 87−91.
32. Poon, M. C.; Ho, C. H.; Deng, F.; Lau, S. S.; Wong, H. Thermal Stability of Cobalt and Nickel Silicides. *Microelectron. Reliab.* **1998**, *38*, 1495–1498.
33. Freitas, W. J.; Swart, J. W. The Influence of Impurities on Cobalt Silicide Formation. *J. Electrochem. Soc.* **1991**, *138*, 3067–3070.
34. Vanderveen, J. F.; Fischer, A.; Vrijmoeth, J. Nickel and Cobalt Silicides on Silicon—Thin-Film Reaction and Interface Structure. *Appl. Surf. Sci.* **1989**, *38*, 13–26.
35. West, G. A.; Beeson, K. W. Chemical Vapor-Deposition of Cobalt Silicide. *Appl. Phys. Lett.* **1988**, *53*, 740–742.
36. Bergholz, W. On the Diffusion of Co in Si and Its Applicability to the Si Intrinsic Defect Problem. *J. Phys. D: Appl. Phys.* **1981**, *14*, 1099–1103.
37. Vangurp, G. J.; Langereis, C. Cobalt Silicide Layers on Si. 1. Structure and Growth. *J. Appl. Phys.* **1975**, *46*, 4301–4307.
38. Alberti, A.; La Via, F.; Raineri, V.; Rimini, E. Thermal Stability of Cobalt Silicide Stripes on Si (001). *J. Appl. Phys.* **1999**, *86*, 3089–3095.
39. Cegiel, M.; Bazarnik, M.; Czajka, R. In *STM Investigation of Cobalt Silicide Nanostructures' Growth on Si(111)-($\sqrt{19} \times \sqrt{19}$) Substrate*, 6th International Cconference on Solid State Surfaces and Interfaces, Smolenice Castle, SLOVAKIA, Nov 24−27, 2008; Versita: Smolenice Castle, Slovakia, 2008; pp 291−294.
40. Tsai, C. I.; Yeh, P. H.; Wang, C. Y.; Wu, H. W.; Chen, U. S.; Lu, M. Y.; Wu, W. W.; Chen, L. J.; Wang, Z. L. Cobalt Silicide Nanostructures: Synthesis, Electron Transport, and Field Emission Properties. *Cryst. Growth Des.* **2009**, *9*, 4514–4518.
41. Chou, Y. C.; Wu, W. W.; Chen, L. J.; Tu, K. N. Homogeneous Nucleation of Epitaxial $CoSi_2$ and NiSi in Si Nanowires. *Nano Lett.* **2009**, *9*, 2337–2342.
42. Chou, Y. C.; Wu, W. W.; Cheng, S. L.; Yoo, B. Y.; Myung, N.; Chen, L. J.; Tu, K. N. *In-situ* TEM Observation of Repeating Events of Nucleation in Epitaxial Growth of Nano $CoSi_2$ in Nanowires of Si. *Nano Lett.* **2008**, *8*, 2194–2199.
43. Qiao, Y. H.; Wang, D.; Buriak, J. M. Block Copolymer Templated Etching on Silicon. *Nano Lett.* **2007**, *7*, 464–469.
44. Zhou, H.; Fu, J.; Silver, R. M. The Influence of Defects on the Morphology of Si (111) Etched in NH_4F. *J. Phys. Chem. B* **2005**, *109*, 23386–23394.

45. Jaccodine, R. J. Surface Energy of Germanium and Silicon. *J. Electrochem. Soc.* **1963**, *110*, 524–527.

46. Hesketh, P. J.; Ju, C.; Gowda, S.; Zanoria, E.; Danyluk, S. Surface Free-Energy Model of Silicon Anisotropic Etching. *J. Electrochem. Soc.* **1993**, *140*, 1080–1085.

47. Ross, F. M.; Bennett, P. A.; Tromp, R. M.; Tersoff, J.; Reuter, M. Growth Kinetics of $CoSi_2$ and Ge Islands Observed with *in situ* Transmission Electron Microscopy. *Micron* **1999**, *30*, 21–32.

48. Goldfarb, I.; Briggs, G. A. D. Reactive Deposition Epitaxy of $CoSi_2$ Nanostructures on Si(001): Nucleation and Growth and Evolution of Dots during Anneal. *Phys. Rev. B* **1999**, *60*, 4800–4809.

49. Bennett, P. A.; Smith, D. J.; Robinson, I. K. Strain in Coherent Cobalt Silicide Islands Formed by Reactive Epitaxy. *Appl. Surf. Sci.* **2001**, *180*, 65–72.

50. Liu, X. H.; Ross, F. M.; Schwarz, K. W. Dislocated Epitaxial Islands. *Phys. Rev. Lett.* **2000**, *85*, 4088–4091.

51. Alloy Phase Diagrams. ASM Handbooks Online, Vol. 3, http://products.asminternational.org/hbk/index.jsp. Accessed November 22, 2009.

52. Lai, S. L.; Carlsson, J. R. A.; Allen, L. H. Melting Point Depression of Al Clusters Generated during the Early Stages of Film Growth: Nanocalorimetry Measurements. *Appl. Phys. Lett.* **1998**, *72*, 1098–1100.

53. Chen, L. J. *Silicide Technology for Intergrated Circuits*; The Institution of Electrical Engineers: London, 2004; pp 19−22.

54. Nogami, J.; Liu, B. Z.; Katkov, M. V.; Ohbuchi, C.; Birge, N. O. Self-Assembled Rare-Earth Silicide Nanowires on Si (001). *Phys. Rev. B* **2001**, *63*, 233305.

55. Chen, Y.; Ohlberg, D. A. A.; Williams, R. S. Nanowires of Four Epitaxial Hexagonal Silicides Grown on Si (001). *J. Appl. Phys.* **2002**, *91*, 3213–3218.

56. Jesson, D. E.; Chen, G.; Chen, K. M.; Pennycook, S. J. Self-Limiting Growth of Strained Faceted Islands. *Phys. Rev. Lett.* **1998**, *80*, 5156–5159.

57. He, Z.; Stevens, M.; Smith, D. J.; Bennett, P. A. Dysprosium Silicide Nanowires on Si (110). *Appl. Phys. Lett.* **2003**, *83*, 5292–5294.

58. Wang, D.; Zou, Z. Q. Formation of Manganese Silicide Nanowires on Si (111) Surfaces by the Reactive Epitaxy Method. *Nanotechnology* **2009**, 20.

59. Comin, F. Room-Temperature Nickel Silicide Nucleation on Si (111) and Si (100). *J. Vac. Sci. Technol., A* **1985**, *3*, 930.

60. Chu, Y. C.; Wu, L. H.; Tsai, C. J. The Growth Kinetics of the Elongated $NiSi_2$ Clusters. *Mater. Chem. Phys.* **2008**, *109*, 271–274.

61. Fernández, L.; Loffler, M.; Cordon, J.; Ortega, J. E. Self-Assembly of Silicide Quantum Dot Arrays on Stepped Silicon Surfaces by Reactive Epitaxy. *Appl. Phys. Lett.* **2007**, *91*, 263106.

62. Famini, S.; Esfandyarpour, B.; Mohajerzadeh, S. Anomalous Anisotropic Etching of (111) and (100) Silicon Wafers Using Acidic Solutions. *J. Electrochem. Soc.* **2006**, *153*, G721–G725.

63. Kretschmer, H. R.; Xia, X. H.; Kelly, J. J.; Steckenborn, A. Anisotropic Etching of Three-Dimensional Shapes in Silicon—The Important Role of Galvanic Interaction. *J. Electrochem. Soc.* **2004**, *151*, C633–C636.

64. Seidel, H.; Csepregi, L.; Heuberger, A.; Baumgartel, H. Anisotropic Etching of Crystalline Silicon in Alkaline-Solutions. 1. Orientation Dependence and Behavior of Passivation Layers. *J. Electrochem. Soc.* **1990**, *137*, 3612–3626.

65. Ueda, K.; Yoshimura, M. Formation of Micromeshes by Nickel Silicide. *Thin Solid Films* **2004**, *464*, 208–210.

66. Huang, W.; Ru, G. P.; Detavernier, C.; Van Meirhaeghe, R. L.; Jiang, Y. L.; Qu, X. P.; Li, B. Z. Yttrium Silicide Formation and Its Contact Properties on Si (100). *Microelectron. Eng.* **2008**, *85*, 131–135.

67. Shen, G. H.; Chen, J. C.; Lou, C. H.; Cheng, S. L.; Chen, L. J. The Growth of Pinhole-free Epitaxial $DySi_{2-x}$ Films on Atomically Clean Si (111). *J. Appl. Phys.* **1998**, *84*, 3630–3635.

68. Barth, J. V.; Costantini, G.; Kern, K. Engineering Atomic and Molecular Nanostructures at Surfaces. *Nature* **2005**, *437*, 671–679.

69. Abraham-Shrauner, B. Simultaneous, Multilayer Plasma Etching and Deposition of Fluorocarbon Layers on Silicon. *J. Appl. Phys.* **2003**, *94*, 4776–4780.

70. Kawashima, T.; Mizutani, T.; Nakagawa, T.; Torii, H.; Saitoh, T.; Komori, K.; Fujii, M. Control of Surface Migration of Gold Particles on Si Nanowires. *Nano Lett.* **2008**, *8*, 362–368.

71. Hawes, E. A.; Hastings, J. T.; Crofcheck, C.; Menguc, M. P. Spatially Selective Melting and Evaporation of Nanosized Gold Particles. *Opt. Lett.* **2008**, *33*, 1383–1385.

72. Lysko, J. M. Anisotropic Etching of the Silicon Crystal-Surface Free Energy Model. *Mater. Sci. Semicond. Process.* **2003**, *6*, 235–241.

73. Bakker, H.; Bonzel, H. P.; Bruff, C. M.; Dayananda, M. A.; Gust, W.; Horvath, J.; Kaur, I.; Kidson, G. V.; Claire, A. D. L.; Mehrer, H.; *et al*. Landolt-Börnstein—Group III Condensed Matter. In *Diffusion in Solid Metals and Alloys*; Mehrer, H., Eds.; Springer-Verlag: Berlin, 1990; Vol. 26, pp 1−2.

74. Heitjans, P.; Kärger, J. *Diffusion in Condensed Matter*; Springer Berlin Heidelberg: New York, 2005; pp 4−5.

75. Weber, T. W.; Chakravo, R. K. Pore and Solid Diffusion Models for Fixed-Bed Adsorbers. *AIChE J.* **1974**, *20*, 228–238.

76. Stearn, A. E.; Eyring, H. Absolute Rates of Solid Reactions: Diffusion. *J. Phys. Chem.* **1940**, *44*, 955–980.

77. Zhang, L.; Du, Y.; Ouyang, Y.; Xu, H.; Lu, X. G.; Liu, Y.; Kong, Y.; Wang, J. Atomic Mobilities, Diffusivities, and Simulation of Diffusion Growth in the Co−Si System. *Acta Mater.* **2008**, *56*, 3940–3950.

78. Hashimoto, K.; Nakashima, H. Diffusion of Electrically-Active Cobalt in Silicon. *Jpn. J. Appl. Phys., Part 1* **1988**, *27*, 1776–1777.

79. Kitagawa, H.; Hashimoto, K. Diffusion-Coefficient of Cobalt in Silicon. *Jpn. J. Appl. Phys.* **1977**, *16*, 173–174.

80. Nakashima, H.; Tomokage, H.; Kitagawa, H.; Hashimoto, K. Energy-Level and Solid Solubility of Cobalt in Silicon by In-Depth Profile Measurement. *Jpn. J. Appl. Phys., Part 1* **1984**, *23*, 776–777.

81. Suwaki, H.; Hashimoto, K.; Nakashima, H. Annealing of Supersaturated Cobalt in Silicon. *Jpn. J. Appl. Phys., Part 1* **1986**, *25*, 1952–1953.